

Selective Oxidation and Reactive Wetting of 1.0 Pct Si-0.5 Pct Al and 1.5 Pct Si TRIP-Assisted Steels

E.M. BELLHOUSE and J.R. McDERMID

The effect of oxygen partial pressure on the selective oxidation and reactive wetting behavior of 1.0 pct Si-0.5 pct Al and 1.5 pct Si TRIP-assisted steels was studied. The annealing atmosphere affected the surface chemistry and the oxide morphology, which in turn affected reactive wetting. Similar wetting results were observed for the two TRIP steel compositions with good wetting being observed at the two lower oxygen partial pressure atmospheres (220 K (−53 °C) or 223 K (−50 °C) dew point (dp) and 243 K (−30 °C) dp) with poor reactive wetting at the higher oxygen partial pressure atmosphere (278 K (+5 °C) dp). The differences in wetting were attributed to the oxide morphology. The predominant oxide morphology at the two low oxygen partial pressure atmospheres was larger, widely spaced oxide nodules. At the 278 K (+5 °C) dp, the predominant oxide morphology was smaller, more closely spaced oxide nodules. TEM analysis revealed that at the 243 K (−30 °C) dp, Fe₂Al₅ was able to form between oxide nodules promoting good reactive wetting. At the 278 K (+5 °C) dp, the more closely spaced nodules may have impeded the formation of Fe₂Al₅, thereby producing numerous bare spot defects in the zinc coating.

DOI: 10.1007/s11661-010-0192-8

© The Minerals, Metals & Materials Society and ASM International 2010

I. INTRODUCTION

IN the automotive industry, there is an increased demand for improved fuel efficiency and decreased greenhouse gas emissions. One method of achieving this objective is by decreasing vehicle weight, but in doing this it is essential that passenger safety not be compromised. TRIP-assisted steels are ideal candidates for automotive lightweighting due to their high strength and ductility, allowing thinner cross sections to be used.^[1,2] Furthermore, at the high strain rates associated with collision events, the energy absorption capabilities of TRIP steels are enhanced, translating to improved passenger safety.^[3,4] For application in parts exposed to the external environment, the continuous galvanizing of TRIP steels is among the most cost effective solutions to provide corrosion protection in order to maintain the structural integrity of the vehicle. However, there are obstacles which must be overcome before these steels can be successfully galvanized. For example, the heat treatment cycles conventionally used for TRIP steels are not necessarily compatible with the thermal cycle used for continuous hot-dip galvanizing. Furthermore, there can also be problems due to the selective oxidation of alloying elements used in these steels, resulting in poor reactive wetting and unacceptable quality coatings.

The conventional heat treatment used for TRIP-assisted steels consists of intercritical annealing (IA) followed by an isothermal bainitic transformation (IBT). Following this heat treatment, the microstructure

should consist of ferrite, bainitic ferrite, high C retained austenite, which transforms to martensite during deformation (the TRIP effect^[5]), and sometimes a small amount of thermal martensite.^[6,7] The high strength of TRIP steels is a result of composite strengthening from the multiphase microstructure, the TRIP effect, and solid solution strengthening by C and Si.^[8–14] IBT temperature typically ranges from 633 K (360 °C) to 723 K (450 °C),^[6,7,10,11,15] and this is problematic for galvanizing as the Zn (Al, Fe) bath is commonly maintained at approximately 733 K (460 °C) and the steel strip entry temperature is usually slightly above this temperature. Increasing the IBT temperature can result in carbide precipitation from the high C retained austenite, thereby lowering the amount and stability of the remaining retained austenite at room temperature.^[16] However, it has been shown that the required microstructures and mechanical properties can be obtained when using IBT temperatures compatible with continuous galvanizing thermal cycles.^[17–19]

The selective oxidation of the alloying elements, Mn, Si, and Al, at the steel surface can result in poor reactive wetting during galvanizing.^[20–24] These oxides can prevent Al in the Zn bath from reacting with metallic Fe on the steel substrate to form the Fe₂Al₅Zn_x interfacial layer, resulting in bare spot defects in the Zn coating and overall poor coating quality. In particular, Si containing oxides on the steel surface have resulted in wettability problems.^[20–22] However, improved galvanizability of Si containing steels has been achieved by increasing the oxygen partial pressure of the annealing atmosphere by using a 247 K (−26 °C) dew point (dp) rather than a 238 K (−35 °C) dp process atmosphere.^[20] In this case, the authors attributed the poor wetting at the 238 K (−35 °C) dp to full coverage of the steel surface by amorphous SiO₂ and the improved wetting observed at the 247 K (−26 °C)

E.M. BELLHOUSE, Doctoral Student, and J.R. McDERMID, Associate Professor, are with the McMaster Steel Research Centre, McMaster University, Hamilton, ON, Canada L8S 4L7. Contact e-mail: mcdermid@mcmaster.ca

Manuscript submitted November 18, 2009.

Article published online April 1, 2010

dp to a sufficient density of holes in the oxide layer. Another technique has been to use a 283 K (+10 °C) dp for heating to the peak annealing temperature, which should promote internal oxidation of alloying elements, followed by lowering the dew point to 223 K (−50 °C) for the remainder of the thermal cycle.^[21] Also, partially or completely replacing Si with Al or P has resulted in improved galvanizability of these steels.^[24–26] It has also been shown that oxide morphology is one factor which is critical for wettability with full coverage of the steel surface with continuous nonporous films resulting in poor wetting.^[20,23]

The objective of the present study is to examine the effect of steel chemistry and processing atmosphere oxygen partial pressure on the reactive wetting of 1.5 wt pct Si and 1.0 wt pct Si-0.5 wt pct Al TRIP-assisted steels. In particular, the effect of these parameters on the steel surface chemistry and oxide morphology and their effect on reactive wetting were explored.

II. EXPERIMENTAL METHOD

The experimental TRIP steel compositions are given in Table I. The steel was cast, hot rolled to a thickness of 4 mm, pickled, sandblasted, and cold rolled to a thickness of approximately 1.5 mm. The hot rolling start and finish temperatures were 1523 K (1250 °C) and 1123 K (850 °C), respectively. Experimental samples comprised 120 mm × 200 mm panels with the longitudinal axis of the sample parallel to the rolling and dipping direction. A uniform temperature and coating area on the panel of 90 mm × 90 mm was centered in the lower portion of the steel panel, and only material from this area was analyzed. Prior to heat treatment, samples were degreased in a 2 pct NaOH solution heated to 353 K (80 °C), rinsed with water, cleaned ultrasonically in isopropanol, and dried with warm air. A final cleaning with acetone was performed immediately prior to the sample entering the galvanizing simulator.

Table I. Experimental TRIP Steel Chemical Composition (Weight Percent)

Alloy Name	C	Mn	Si	Al	Ti
1.0 pct Si	0.21	1.52	1.08	0.49	0.02
1.5 pct Si	0.20	1.50	1.47	0.006	0.018

All annealing and galvanizing experiments were carried out in the McMaster Galvanizing Simulator, details of which are provided elsewhere.^[27] The heat treatment consisted of heating at 10 K s^{−1} to the IA temperature, holding at the IA temperature for 120 seconds, cooling at 20 K s^{−1} to the IBT temperature of 738 K (465 °C), holding at 738 K or 120 seconds, and rapid cooling to room temperature. The IA temperature was 1070 K (797 °C) for the 1.0 pct Si steel and 1050 K (777 °C) for the 1.5 pct Si steel. These IA temperatures were chosen to produce an intercritical microstructure of 50 pct α -50 pct γ (vol pct) and were determined using ThermoCalc software and the TCFE2 database (Thermo-Calc Software, Stockholm, Sweden). Samples that were galvanized were dipped for 4 seconds in the Zn bath following 116 seconds of the 120-second IBT hold. The Zn bath was held at 733 K (460 °C) and contained 0.2 wt pct dissolved Al and was Fe saturated.^[28]

Three different annealing atmospheres were tested, as shown in Table II, to determine the effect of oxygen partial pressure on selective oxidation and galvanizing behavior. These annealing atmospheres will be distinguished by their dew point in the subsequent text. Oxygen partial pressure is strongly temperature dependent and was calculated as a function of steel IA temperature (1070 K (797 °C) for the 1.0 pct Si TRIP steel and 1050 K (777 °C) for the 1.5 pct Si TRIP steel) using the thermodynamic data of Fine and Geiger^[29] (Table II). It should be noted that samples will be referred in the subsequent text per the sample name given in Table II.

Samples that were subjected to the annealing cycle without galvanizing in order to analyze the selective oxidation of the steel surface were polished to remove the effect of surface roughness. Samples analyzed with X-ray photoelectron spectroscopy (XPS) were polished prior to annealing with 4000 grit SiC paper as the final step. For analysis of the oxide morphology by scanning electron microscopy (SEM) and to determine the elemental distribution of the steel surface by scanning Auger microscopy (SAM), the steel was polished to 0.05 μ m prior to annealing. After annealing and prior to analysis with XPS, SEM, and SAM, samples were stored in anhydrous isopropanol to minimize further oxidation of the surface.

Chemical analysis of the steel surface was determined using XPS. XPS analysis was performed using a PHI Quantera X-ray photoelectron spectroscope with an Al

Table II. Annealing Atmosphere Compositions

Steel and Process Atmosphere Name	Dew Point K (°C)	N ₂ Content (Vol Pct)	H ₂ Content (Vol Pct)	pO ₂ at IA Temperature (1070 K for 1.0 Pct Si, 1050 K for 1.5 Pct Si) (Atm)
1.0 pct Si −50 °C dp	223 (−50)	80	20	4.13×10^{-26}
1.0 pct Si −30 °C dp	243 (−30)	95	5	4.05×10^{-23}
1.0 pct Si +5 °C dp	278 (+5)	95	5	1.41×10^{-20}
1.5 pct Si −53 °C dp	220 (−53)	80	20	7.16×10^{-27}
1.5 pct Si −30 °C dp	243 (−30)	95	5	1.40×10^{-23}
1.5 pct Si +5 °C dp	278 (+5)	95	5	3.95×10^{-21}

K_{α} X-ray source (Physical Electronics, Chanhassen, MN). The spot size used was 100 μm and the take off angle was 45 deg. All spectra were calibrated using the metallic iron peak position at 706.62 eV. The binding energy values obtained were accurate to within ± 0.1 eV, and the accuracy of the chemical composition measurements are ± 5 pct of the measured value in atomic percent for each element. The XPS results shown were collected after sputtering with Ar to a depth of approximately 5 nm.

Oxide morphology was determined using SEM. SEM analysis was performed using a JEOL* 7000F field

*JEOL is a trademark of Japan Electron Optics Ltd., Tokyo.

emission scanning electron microscope. An acceleration voltage of 7 keV was used for all samples. Samples were sputter coated with gold to avoid sample charging. The correlation between oxide morphology and elemental distribution was studied with elemental mapping using SAM. SAM data was collected using a JEOL JAMP-9500F field emission Auger microprobe. The energy of the primary electron beam was 15 keV for all samples with the exception of the 1.0 pct Si +5 °C dp steel where 10 keV was used. The samples were tilted at 30 deg toward the electron analyzer. Auto probe tracking was in effect during the collection of elemental maps to eliminate sample drift. The signal intensity (I) was calculated using Eq. [1] to attenuate the effect of topography.

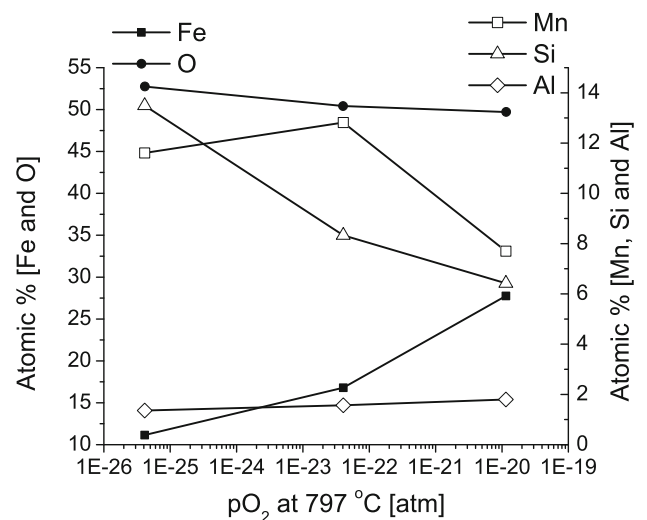
$$I = \frac{\text{peak} - \text{background}}{\text{background}} \quad [1]$$

Auger maps were collected at the steel surface and after Ar sputtering. The accuracy of the sputtering depth was ± 10 pct.

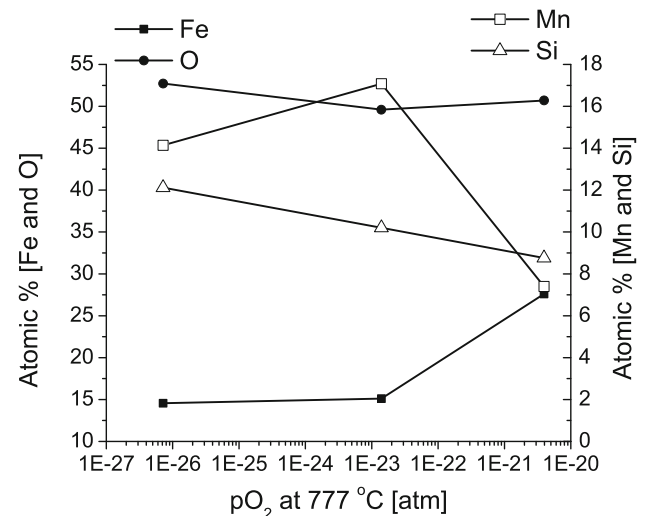
Reactive wetting of the steels by the liquid Zn bath was studied by counting and measuring the area of bare spots in the galvanized coating within the uniform temperature and coating area. Measurement of bare spots on the galvanized panels was performed using a Carl Zeiss Ltd. Stemi 2000-C stereoscope (Carl Zeiss Canada Ltd., Toronto, ON, Canada) and Northern Eclipse Version 6.0 image analysis software by Empix Imaging Inc. (Empix Imaging, Inc., Mississauga, ON, Canada) Images were captured using a magnification of 5 \times . The bare spot area was measured by manually selecting the bare spot perimeter. The measured bare spot area is accurate to within ± 0.01 mm².

The reactive wetting behavior was also investigated by analyzing the steel/coating interface *via* SEM and transmission electron microscopy (TEM). An SEM acceleration voltage of 10 keV was used for all samples with the exception of the 1.5 pct Si +5 °C dp steel where 5 keV was used. The interfacial layer on the galvanized panels was exposed for SEM analysis by two methods: (1) stripping the zinc overlay with 10 vol pct H₂SO₄ in water, which leaves both the Fe-Al and Fe-Zn intermetallics intact; and (2) stripping with fuming HNO₃, which strips the zinc overlay and Fe-Zn intermetallics. TEM was performed with a JEOL 2010F TEM equipped with an Oxford INCA Pentafet energy

dispersive X-ray (EDX) spectrometer (Oxford Instruments, Abingdon, Oxfordshire, UK). The acceleration voltage was 200 keV. EDX was performed in scanning transmission electron microscopy (STEM) mode with a probe size of 1 nm. TEM sample preparation was performed using focused ion beam (FIB) milling with an NVision 40 by Zeiss. Carbon was deposited over the FIB sample location as Zn is sputtered more easily than Fe and the carbon layer minimized the preferential thinning of the Zn overlay. Carbon deposition also decreased the likelihood of the sample breaking during fabrication in the case of a sample made at the edge of a bare spot, as this sample was particularly fragile due to the obtuse contact angle between the Zn and the substrate (shown in Figure 12(a)).



(a)



(b)

Fig. 1—Chemical composition of the steel surface after annealing as determined with XPS (5 nm sputtering) (a) 1.0 pct Si steel and (b) 1.5 pct Si steel.

III. RESULTS

A. Surface Oxidation and Oxide Morphology

Figures 1(a) and (b) show the chemical composition of the steel surface determined *via* XPS plotted as a function of oxygen partial pressure during IA for the 1.0 pct Si and 1.5 pct Si steels, respectively. Considerable surface enrichment of oxygen, silicon, and manganese was observed for all annealing atmospheres and both steels. The two steels showed similar behaviors in terms of the relative enrichments of Si and Mn with respect to oxygen partial pressure. The 1.0 pct Si steel, which also had 0.5 wt pct Al in the bulk composition, did not show significant Al enrichment at the steel surface. Table III lists the binding energies of the elements of interest and oxides identified on the steel surface, from which it can be seen that the oxygen partial pressure affected the surface composition as well as the oxides present. It should be noted that for the 1.0 pct Si TRIP steel at the $-50\text{ }^{\circ}\text{C}$ dp no binding energy for Al is listed because no clear Al peak was identified. The decreasing Si binding energy that is observed with increasing dew point for both steel compositions indicates a decrease in the amount of SiO_2 at the steel surface with Si in the form of Mn_2SiO_4 being favored. This is in agreement with the decreasing amount of Si observed at the surface (Figure 1).

The link between oxide morphology and chemistry was determined by SAM. Elemental mapping of the steel surface and corresponding secondary electron images are shown in Figures 2 through 7. Figures 2 through 4 are for the 1.0 pct Si steel at the $-50\text{ }^{\circ}\text{C}$ dp, $-30\text{ }^{\circ}\text{C}$ dp, and $+5\text{ }^{\circ}\text{C}$ dp, respectively. Figures 5 through 7 are for the 1.5 pct Si steel at the $-53\text{ }^{\circ}\text{C}$ dp, $-30\text{ }^{\circ}\text{C}$ dp, and $+5\text{ }^{\circ}\text{C}$ dp, respectively. Elemental maps for Fe, O, Mn, and Si were collected for both steel chemistries; Al maps were also collected for the 1.0 pct Si steel. Elemental maps were collected at the steel surface and after sputtering with Ar. In general, the results were very similar when comparing the elemental maps before and after sputtering, except for the 1.5 pct Si $-53\text{ }^{\circ}\text{C}$ dp and $-30\text{ }^{\circ}\text{C}$ dp steels, where many details were only revealed after sputtering to a depth of 20 nm. Thus, all maps shown are for the steel surface with the exception of the 1.5 pct Si $-53\text{ }^{\circ}\text{C}$ dp and $-30\text{ }^{\circ}\text{C}$ dp samples, where maps of the sample surface before and after sputtering are shown (Figures 5 and 6). The Al map is not shown for 1.0 pct Si $-50\text{ }^{\circ}\text{C}$ dp and $+5\text{ }^{\circ}\text{C}$ dp

samples as no Al rich features were found. It should be noted that Fe should not be oxidized during annealing prior to galvanizing and that any oxidation of Fe likely occurred upon removal of the sample from the galvanizing simulator. XPS analysis revealed that any Fe oxides were very thin (approximately 5 nm), which is considerably thinner than the oxidized layer for the alloying elements. SEM analysis of the steel surface of the 1.5 pct Si $-53\text{ }^{\circ}\text{C}$ dp sample is shown in Figure 8 at a higher magnification than is shown in Figure 5(a) to show the oxide morphology in greater detail.

B. Reactive Wetting

The reactive wetting behavior was analyzed by three methods: bare spot analysis of the galvanized panels, analysis of the interfacial reaction products with SEM, and analysis of the cross section of the steel/coating interface with TEM. The bare spot analysis is summarized in Table IV. For both steel compositions, the two lower oxygen partial pressure atmospheres (223 K ($-50\text{ }^{\circ}\text{C}$) dp or 220 K ($-53\text{ }^{\circ}\text{C}$) dp and 243 K ($-30\text{ }^{\circ}\text{C}$) dp) resulted in good wetting with only a few bare spots present in the galvanized coating and a small total bare area. At the 278 K ($+5\text{ }^{\circ}\text{C}$) dp, poor wetting was observed for both steel compositions with a large number of bare spots in the uniform temperature and coating area and a considerably larger total bare area.

SEM analysis of the steel/coating interface is shown in Figures 9 and 10. For both steel chemistries and at all three annealing atmospheres, Fe_2Al_5 and FeZn_{13} were present at the iron-zinc interface. The presence of Fe_2Al_5 indicates that good reactive wetting occurred during galvanizing. FeZn_{13} is not expected when galvanizing using a Zn bath with 0.2 wt pct dissolved Al. Qualitative analysis of the images obtained shows that for both steel chemistries there was more FeZn_{13} present at the interface when using the 287 K ($+5\text{ }^{\circ}\text{C}$) dp atmosphere (Figures 9 and 10(c)). In Figure 10(a), some interesting features were observed regarding the growth of FeZn_{13} relative of Fe_2Al_5 , where FeZn_{13} is shown growing on top of Fe_2Al_5 grains as well as growing around Fe_2Al_5 grains.

Cross sections of the steel/coating interface were analyzed with TEM EDX mapping (Figures 11 through 14) and quantitative EDX analysis of points indicated by the letters a through g in Figures 11 through 14(a)

Table III. Identification of Oxides on the Steel Surface using XPS

Steel and Atmosphere	Measured Binding Energies (eV)					Oxides Present
	Al 2p	Mn 2p _{3/2}	Mn 2p _{1/2}	Si 2p	O 1s	
1.0 pct Si $-50\text{ }^{\circ}\text{C}$ dp	—	642.7	654.5	103.4	532.3	SiO_2 , ^[30–33] Mn_2SiO_4 ^[31–34]
1.0 pct Si $-30\text{ }^{\circ}\text{C}$ dp	74.3	642.3	654.2	102.7	531.6	Al_2O_3 , ^[35] MnO , ^[35] SiO_2 , Mn_2SiO_4
1.0 pct Si $+5\text{ }^{\circ}\text{C}$ dp	74.1	642.0	654.0	102.3	530.9	Al_2O_3 , MnO , Mn_2SiO_4
1.5 pct Si $-53\text{ }^{\circ}\text{C}$ dp	—	642.4	654.1	102.8	531.6	SiO_2 , Mn_2SiO_4
1.5 pct Si $-30\text{ }^{\circ}\text{C}$ dp	—	642.3	654.3	102.6	531.5	MnO , SiO_2 , Mn_2SiO_4
1.5 pct Si $+5\text{ }^{\circ}\text{C}$ dp	—	642.0	654.0	102.4	531.2	MnO , Mn_2SiO_4

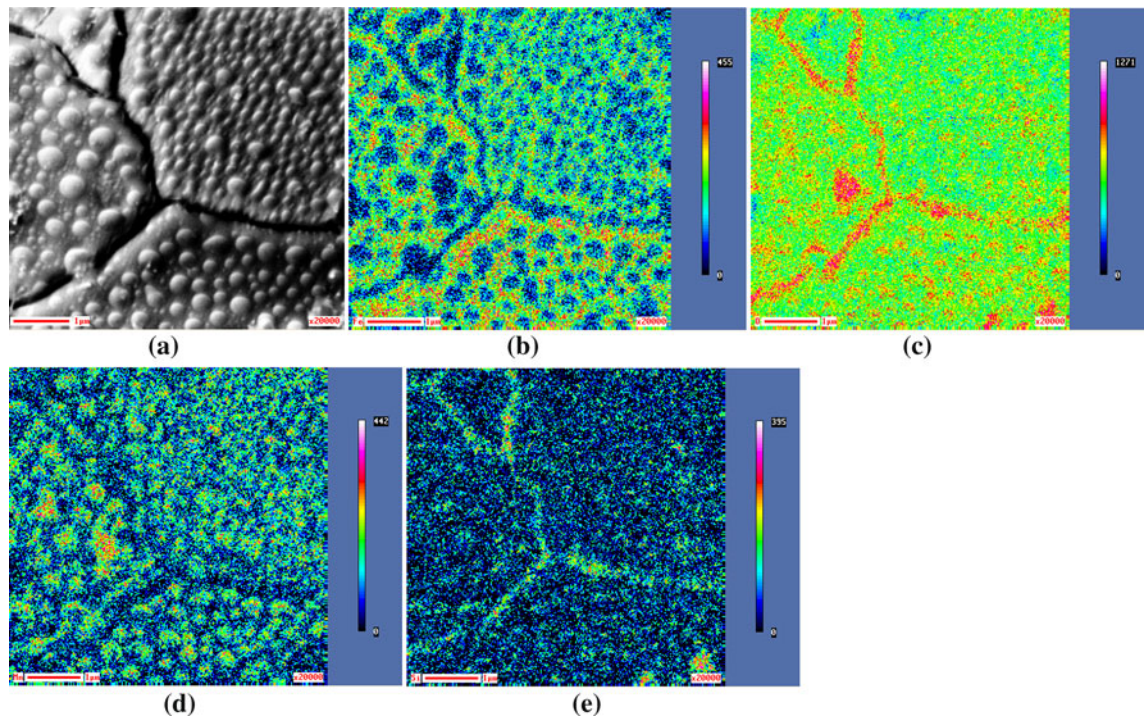


Fig. 2—Oxide morphology of the 1.0 pct Si $-50\text{ }^{\circ}\text{C}$ dp steel using Auger mapping of the steel surface (a) Secondary electron image, (b) Fe, (c) O, (d) Mn, and (e) Si maps.

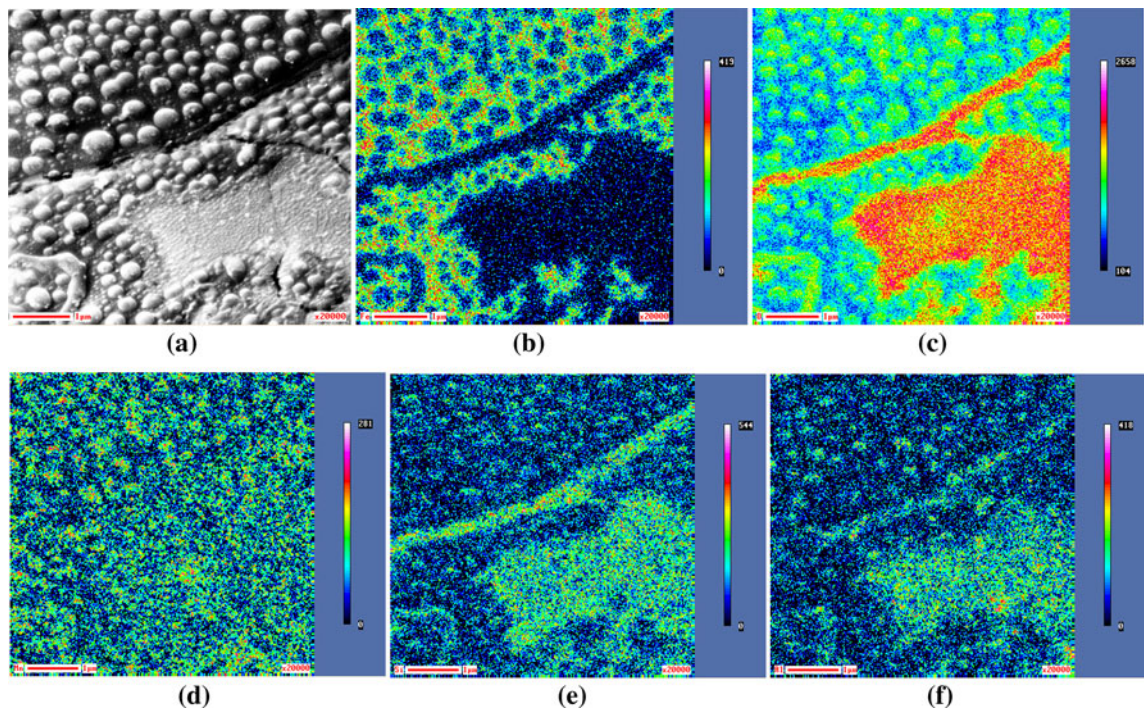


Fig. 3—Oxide morphology of the 1.0 pct Si $-30\text{ }^{\circ}\text{C}$ dp steel using Auger mapping of the steel surface (a) Secondary electron image, (b) Fe, (c) O, (d) Mn, (e) Si, and (f) Al maps.

(Table V). For the 1.0 pct Si steel, two samples were analyzed: the $-30\text{ }^{\circ}\text{C}$ dp (Figure 11) where good reactive wetting was observed and the $+5\text{ }^{\circ}\text{C}$ dp (Figures 12 and 13) where a sample was made at the edge of a bare

spot in the Zn overlay showing the transition from wetting to nonwetting. The 1.5 pct Si $-30\text{ }^{\circ}\text{C}$ dp steel, which showed good reactive wetting, was also analyzed (Figure 14).

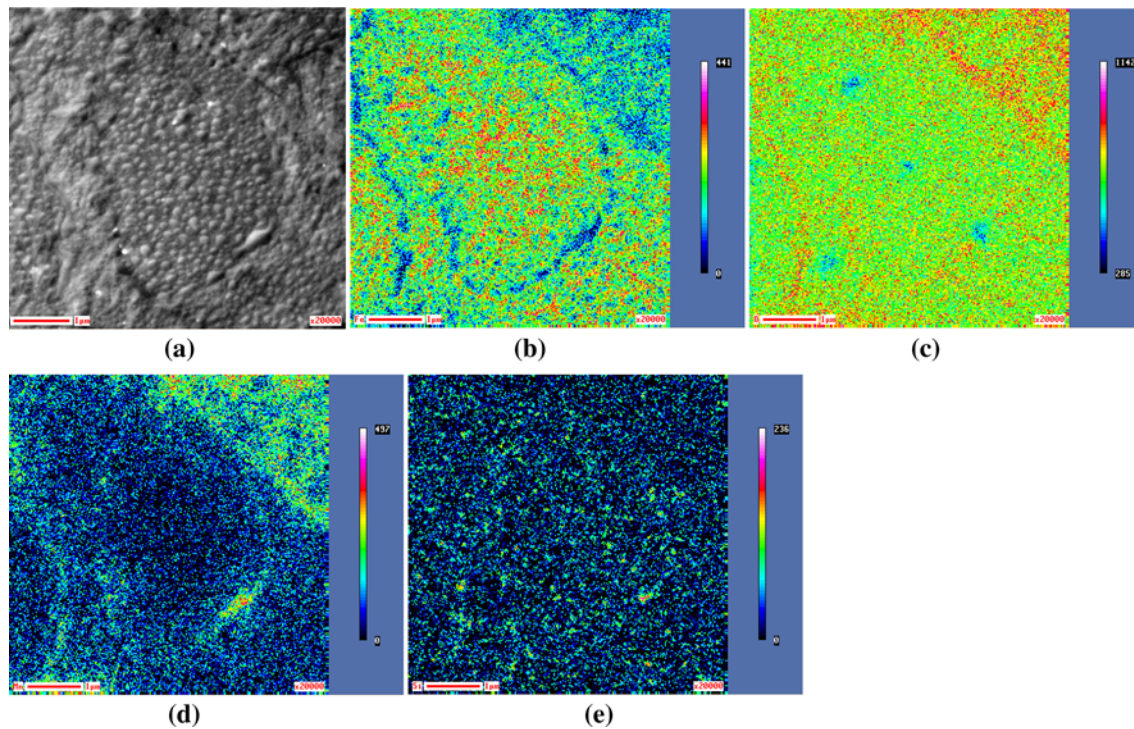


Fig. 4—Oxide morphology of the 1.0 pct Si +5 °C dp steel using Auger mapping of the steel surface (a) Secondary electron image, (b) Fe, (c) O, (d) Mn, and (e) Si maps.

For the 1.0 pct Si –30 °C dp sample, an Al rich layer is present at the steel/coating interface (Figure 11(f)). Mn and Si rich oxides remained at and below the steel surface (Figure 11(c) through (e)); the compositions of these oxides are shown in Table V (point a in Figure 11(a)). It can be seen that the Al rich layer formed between oxide particles. Over the Al rich interfacial layer, there were Fe-Zn intermetallics (Figure 11(a) and Table V point b). The oxide particles reached a depth of approximately 300 nm below the steel surface, as shown in Figure 11(a).

The transition between wetting and nonwetting is shown in the 1.0 pct Si +5 °C dp sample (Figure 12). At the start of the area where poor wetting occurred, indicated in Figure 12(a), there were Mn and Si rich oxides at and below the surface, likely the cause of the poor wetting observed. The composition of the subsurface oxide particle, point c in Figure 12(a), is shown in Table V. The Al rich interfacial layer is present in the area of this sample where good reactive wetting occurred (top half of Figure 12(a) and (f)), but it did not extend into the bare spot. The hole in the sample to the right of the Zn (shown in Figure 12(g)) is an artefact of sample preparation due to preferential sputtering of the Zn and is not associated with the bare spot.

Figure 13 shows an area within the bare spot analyzed on the 1.0 pct Si +5 °C dp sample. At the steel surface, there is material that was redeposited during FIB sample preparation; this region is indicated in Figure 13(a). Many Mn and Si rich oxides are present between 400 nm and 1 μm below the steel surface (Figure 13(c)

through (e)); the composition of one of these oxides, indicated by point d in Figure 13(a), is shown in Table V. There was also a Mn and Si rich oxide layer at the steel surface (Figure 13(c) through (e)). This surface oxide layer was likely the cause of poor reactive wetting in this region.

For the 1.5 pct Si –30 °C dp steel, shown in Figure 14, Mn and Si rich oxides were present at and below the surface (Figure 14(c) through (e)). The composition of the oxides below the steel surface, indicated by points e and f in Figure 14(a), is shown in Table V. There was an Al rich layer at the Fe-Zn interface (Figure 14(f)); the composition of one of these Al rich grains, indicated by g in Figure 14(a), is shown in Table V. The Al rich interfacial layer formed around the oxide particles, as shown by comparing Figures 14(d) and (f).

IV. DISCUSSION

A. Surface Oxidation and Oxide Morphology

During annealing prior to galvanizing, considerable enrichment of Mn and Si in the form of oxides was observed at the steel surface for both steel chemistries and all annealing atmospheres (Figure 1 and Table III). Furthermore, the oxygen partial pressure of the annealing atmosphere had a significant effect on the surface chemistry and on the oxide morphology for all the steels examined (Figures 1 through 7). Similar trends in surface chemistry were observed when comparing the two TRIP steels (Figure 1). As the oxygen partial

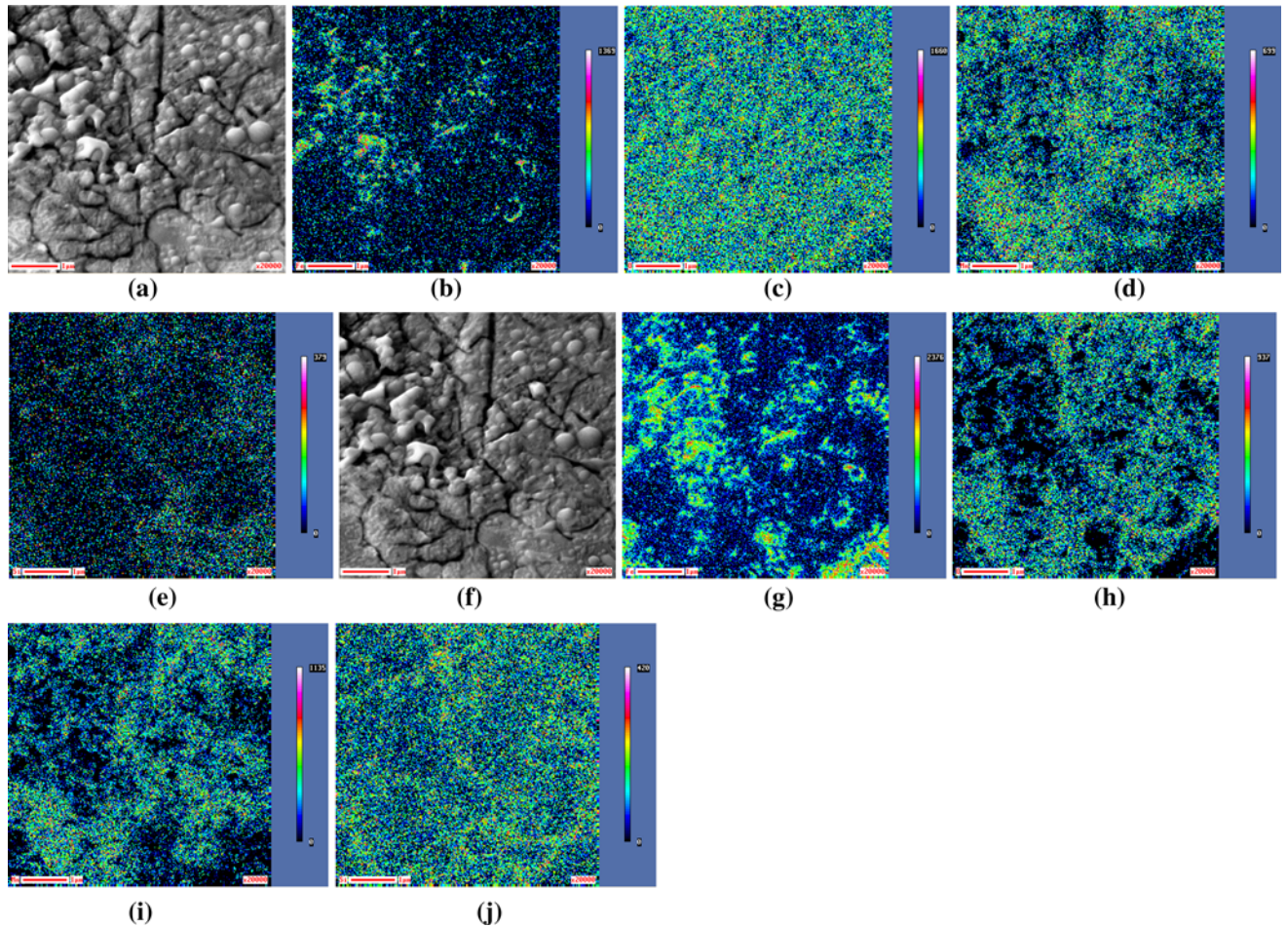


Fig. 5—Oxide morphology of the 1.5 pct Si -53°C dp steel using Auger mapping (a) through (e) are for the steel surface, (a) Secondary electron image, (b) Fe, (c) O, (d) Mn, and (e) Si maps, (f) through (j) are for after sputtering 20 nm below the surface, (f) Secondary electron image, (g) Fe, (h) O, (i) Mn, and (j) Si maps.

pressure of the annealing atmosphere was increased, the amount of Si at the steel surface decreased regardless of steel chemistry. For both steel chemistries, the maximum Mn surface enrichment was observed at the 243 K (-30°C) dp. Furthermore, the amount of Fe at the steel surface increased as the oxygen partial pressure of the annealing atmosphere was increased; this coincides with a decrease in Mn and Si segregation to the surface at the 278 K ($+5^{\circ}\text{C}$) dp, indicative of internal oxidation of the alloying elements.

For the 1.0 pct Si $+5^{\circ}\text{C}$ dp steel, internal oxidation was observed by TEM EDX mapping (Figure 13). When comparing the subsurface oxidation of the 1.0 pct Si -30°C dp (Figure 11) and $+5^{\circ}\text{C}$ dp (Figure 13) steels, oxide particles penetrated to a much greater depth at the $+5^{\circ}\text{C}$ dp than they did at the -30°C dp. At the $+5^{\circ}\text{C}$ dp, many oxides were present 400 nm to 1 μm below the surface (Figure 13(a)), whereas oxide particles reached a maximum depth of 300 nm below the surface in the -30°C dp (Figure 11(a)).

Internal oxidation is expected at higher oxygen partial pressures, as predicted by the Wagner model for the transition between internal and external oxidation.^[36] The conditions that result in the transition between

internal and external oxidation using extensions of the Wagner model have been calculated previously for various Si, Mn, and Al containing steel chemistries by several authors.^[37–40] At the 278 K ($+5^{\circ}\text{C}$) dp, bulk internal oxidation of the alloying elements is expected with external oxidation at the grain boundaries (recalculated for the alloys and IA temperatures in the present work using elements of the existing models and the appropriate diffusion data).^[37,38,41–46]

External oxidation was still observed for the 1.0 pct Si $+5^{\circ}\text{C}$ dp and 1.5 pct Si $+5^{\circ}\text{C}$ dp steels (Figures 1, 4, and 7). For the 1.0 pct Si steel, Mn and Si enrichment occurred at the surface in the form of oxide nodules and grain boundary oxidation (Figure 4(d) and (e)). For the 1.5 pct Si steel, Mn rich oxides were observed at the grain boundaries and Si oxidation occurred for the entire steel surface (Figure 7(a) and (e)). One reason for the discrepancy between the predicted and experimental results could be the high solubility product of MnO , which was not taken into consideration in the model used. The effect of oxide solubility product is discussed in detail by Huin *et al.*^[40]

The oxide morphology was studied with scanning Auger microscopy (Figures 2 through 7). The oxide

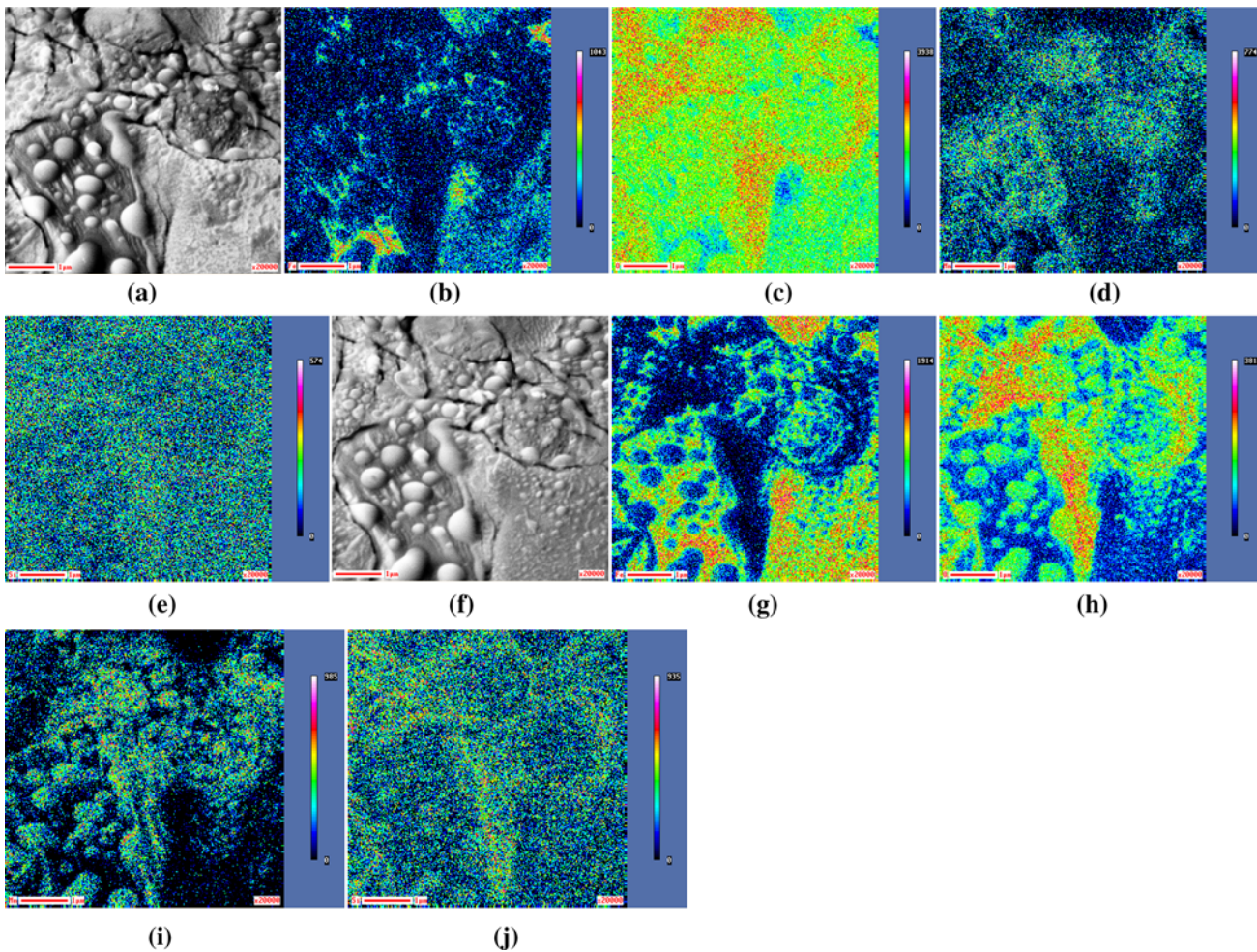


Fig. 6—Oxide morphology of the 1.5 pct Si -30°C dp steel using Auger mapping (a) through (e) are for the steel surface, (a) Secondary electron image, (b) Fe, (c) O, (d) Mn and (e) Si maps, (f) through (j) are for after sputtering 20 nm below the surface, (f) Secondary electron image, (g) Fe, (h) O, (i) Mn, and (j) Si maps.

morphology was affected by the oxygen partial pressure and chemical composition of the TRIP steel. For the 1.0 pct Si -50°C dp and -30°C dp steels, the predominant oxide surface morphology was large, relatively widely spaced oxide nodules (Figures 2 and 3). At the -30°C dp, there were also small closely spaced nodules that formed a film (Figure 3). At the -50°C dp, the oxide nodules were rich in Mn and Si (Figure 2(d) and (e)), whereas at the -30°C dp, both large and small nodules were rich in Mn, Si, and Al (Figure 3(d) through (f)). The oxide morphology was significantly different for the 1.0 pct Si $+5^{\circ}\text{C}$ dp steel, with smaller, more closely spaced oxide nodules covering the steel surface (Figure 4). These oxide nodules were rich in Mn and Si (Figure (d) and (e)).

There was also significant oxidation in the grain boundaries for the 1.0 pct Si steel, where the oxide chemistry varied with oxygen partial pressure (Figures 2 through 4). Figure 2(e) shows that the grain boundary oxides were rich in Si, likely in the form of SiO_2 at the -50°C dp, whereas at the -30°C dp, the grain boundaries were rich in Si and Al (Figure 3(e) and (f)). Conversely, at

the $+5^{\circ}\text{C}$ dp, the grain boundaries were rich in Mn with some Si also being observed (Figure 4(d) and (e)).

For the 1.5 pct Si -53°C dp steel, a mixture of large and small nodule type oxides were identified at the steel surface (Figures 5 and 8). In the SEM image at higher magnification (Figure 8), the fine detail of the smaller nodules is clear and an oxide network incorporating larger oxide nodules is also visible. Very little Fe was observed at the steel surface (Figure 5(b)), indicating that Mn and Si oxides almost completely covered the surface. However, the Fe concentration was higher 20 nm below the steel surface (Figure 5(g)) indicating that in some areas the oxide layer was quite thin. Despite the small amount of Fe at the steel surface, good reactive wetting was observed at the -53°C dp (Table V and Figure 10(a)). Good reactive wetting was attributed to the relatively larger area fraction of thinner oxide areas. Si and Mn surface enrichment was not coincident, as shown by comparing Figure 5(d) and (e) and Figure 5(i) and (j). In particular, Si rich oxides were observed at the grain boundaries, as shown after sputtering (Figure 5(j)).

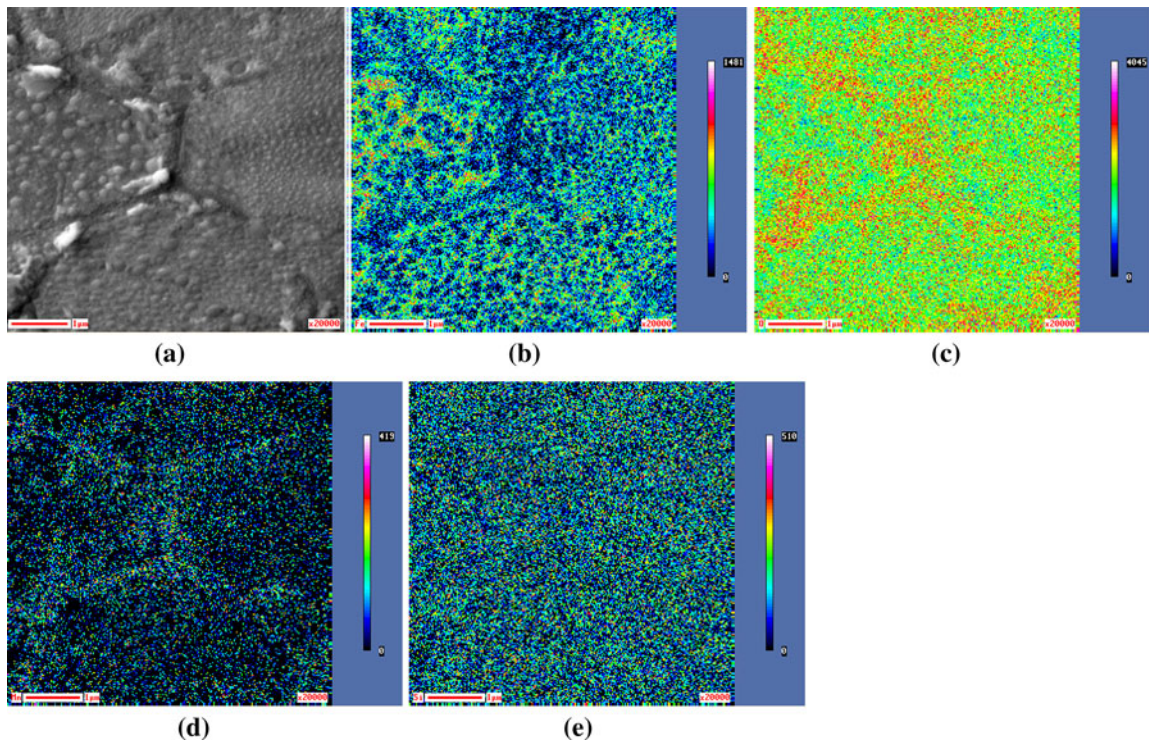


Fig. 7—Oxide morphology of the 1.5 pct Si +5 °C dp steel using Auger mapping of the steel surface (a) Secondary electron image, (b) Fe, (c) O, (d) Mn, and (e) Si maps.

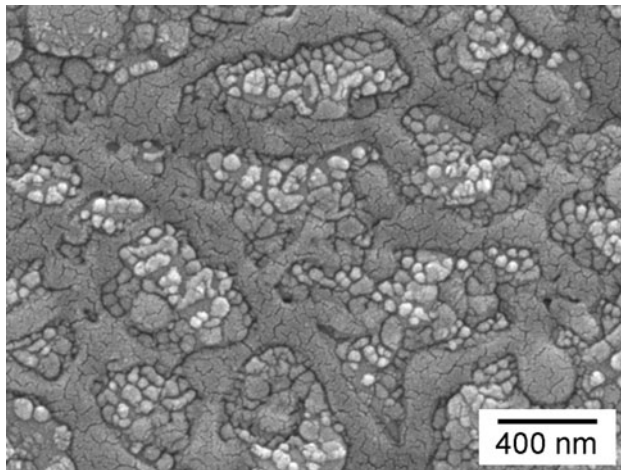


Fig. 8—SEM image of the 1.5 pct Si -53 °C dp steel surface after annealing.

For the 1.5 pct Si -30 °C dp sample, the oxide morphology was a mixture of large nodules, small nodules that formed film type oxides, and Si rich oxide films between the large oxide nodules (Figure 6). The large nodules were rich in Mn (Figure 6(d) and (i)). Si was present at the grain boundaries, film type oxides (lower right and upper left of Figure 6(e) and (j)), and also in the nodules. The difference in oxide morphology with respect to different grains could be due to the two phase intercritical microstructure, as the diffusivities of oxygen, manganese, and silicon are different in ferrite

Table IV. Bare Spot Analysis

Sample Name	Number of Bare Spots	Average Bare Spot Size (mm ²)	Total Bare Area* (mm ²)
1.0 pct Si -50 °C dp	6	0.24	1.46
1.0 pct Si -30 °C dp	1	0.37	0.37
1.0 pct Si +5 °C dp	443	0.47	209.28
1.5 pct Si -53 °C dp	1	0.50	0.50
1.5 pct Si -30 °C dp	11	0.12	1.35
1.5 pct Si +5 °C dp	211	0.52	110.72

*The total area analyzed was 8100 mm².

and austenite.^[43–46] When comparing the present results to those of Gong *et al.*,^[47] who studied the effect of annealing temperature on oxide morphology on a TRIP steel of similar chemical composition in a 243 K (-30 °C) dp atmosphere, it is likely that the grains with large oxide nodules were ferrite during IA and the grains with the small nodule/film type oxide were austenite. However, it should be pointed out that Gong *et al.*^[47] used a considerably longer annealing time than was used in the present work.

For the 1.5 pct Si +5 °C dp steel, the oxide morphology comprised small, closely spaced nodules. The entire surface was covered in a Si rich oxide (Figure 7(c) and (e)) and the grain boundaries were rich in Mn (Figure 7(d)).

Similar trends in oxide morphology are observed in both TRIP steel compositions when increasing the annealing atmosphere oxygen partial pressure. At the

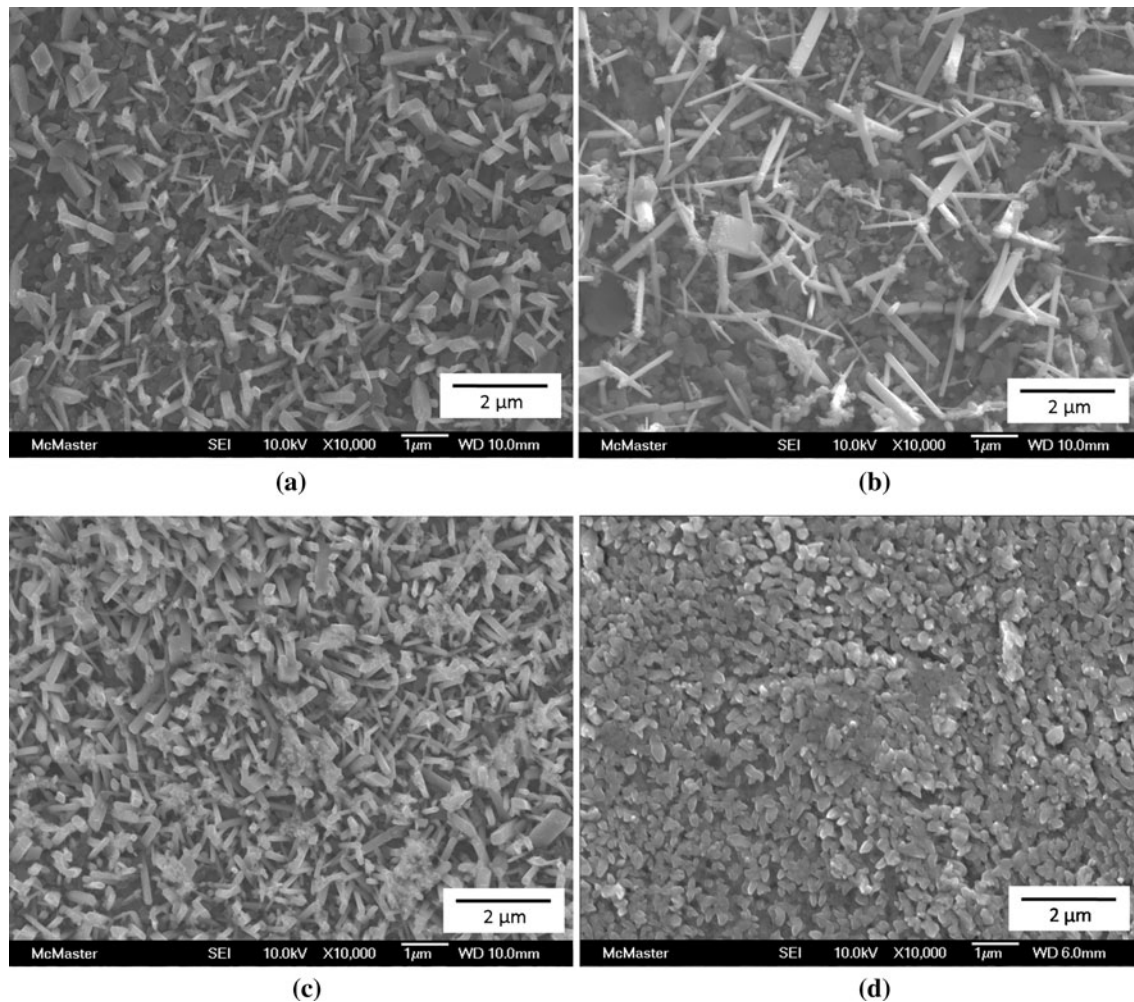


Fig. 9—SEM analysis of the steel/coating interface for the 1.0 pct Si steel (a) $-50\text{ }^{\circ}\text{C}$ dp, (b) $-30\text{ }^{\circ}\text{C}$ dp, (c) and (d) $+5\text{ }^{\circ}\text{C}$ dp, (a) through (c) were stripped with 10 pct H_2SO_4 and (d) was stripped with HNO_3 .

$+5\text{ }^{\circ}\text{C}$ dp, only small, closely spaced oxide nodules were observed; this morphology was different when compared to those obtained at the lower oxygen partial pressure atmospheres (comparison of Figures 4 and 7 to Figures 2, 3, 5, 6, and 8). Also, Mn oxidation was observed in the grain boundaries at the $+5\text{ }^{\circ}\text{C}$ dp, whereas the grain boundaries were rich in Si (and Al for the 1.0 pct Si $-30\text{ }^{\circ}\text{C}$ dp steel) for the lower oxygen partial pressure atmospheres.

B. Reactive Wetting

The reactive wetting behavior of the two steel chemistries was similar with respect to the annealing atmosphere oxygen partial pressure. Both steels showed good reactive wetting at the two low oxygen partial pressure atmospheres (220 K ($-53\text{ }^{\circ}\text{C}$) dp or 223 K ($-50\text{ }^{\circ}\text{C}$) dp and 243 K ($-30\text{ }^{\circ}\text{C}$) dp) and poor wetting at 278 K ($+5\text{ }^{\circ}\text{C}$) dp. Comparing the interfacial reaction products, Fe_2Al_5 and FeZn_{13} were observed for both steel chemistries and all three annealing atmospheres tested (Figures 9 and 10). Fe_2Al_5 was not visible on the $+5\text{ }^{\circ}\text{C}$ dp samples when stripping the Zn overlay with

10 pct H_2SO_4 due to the large amount of FeZn_{13} (Figures 9 and 10(c)), but Fe_2Al_5 was observed on these samples when stripping the Zn overlay with HNO_3 (Figures 9 and 10(d)). However, the Fe_2Al_5 layer was not continuous on the 1.5 pct Si $+5\text{ }^{\circ}\text{C}$ dp steel (Figure 10(d)). The presence of FeZn_{13} is symptomatic of a localized Al depletion in the Zn bath by a reaction which preferentially consumes Al at the expense of Fe_2Al_5 , for example, aluminothermic reduction of surface oxides. The reduction of a MnO film was shown to be thermodynamically possible in a 0.2 wt pct Al bath by Khondker *et al.*,^[48] per the reaction shown in Eq. [2].



Furthermore, the aluminothermic reduction of manganese silicates *via* the reaction shown in Eq. [3] was proposed by Gong *et al.*^[49]



It should be noted that Al in the mass transport boundary layer may not be renewed during dipping due

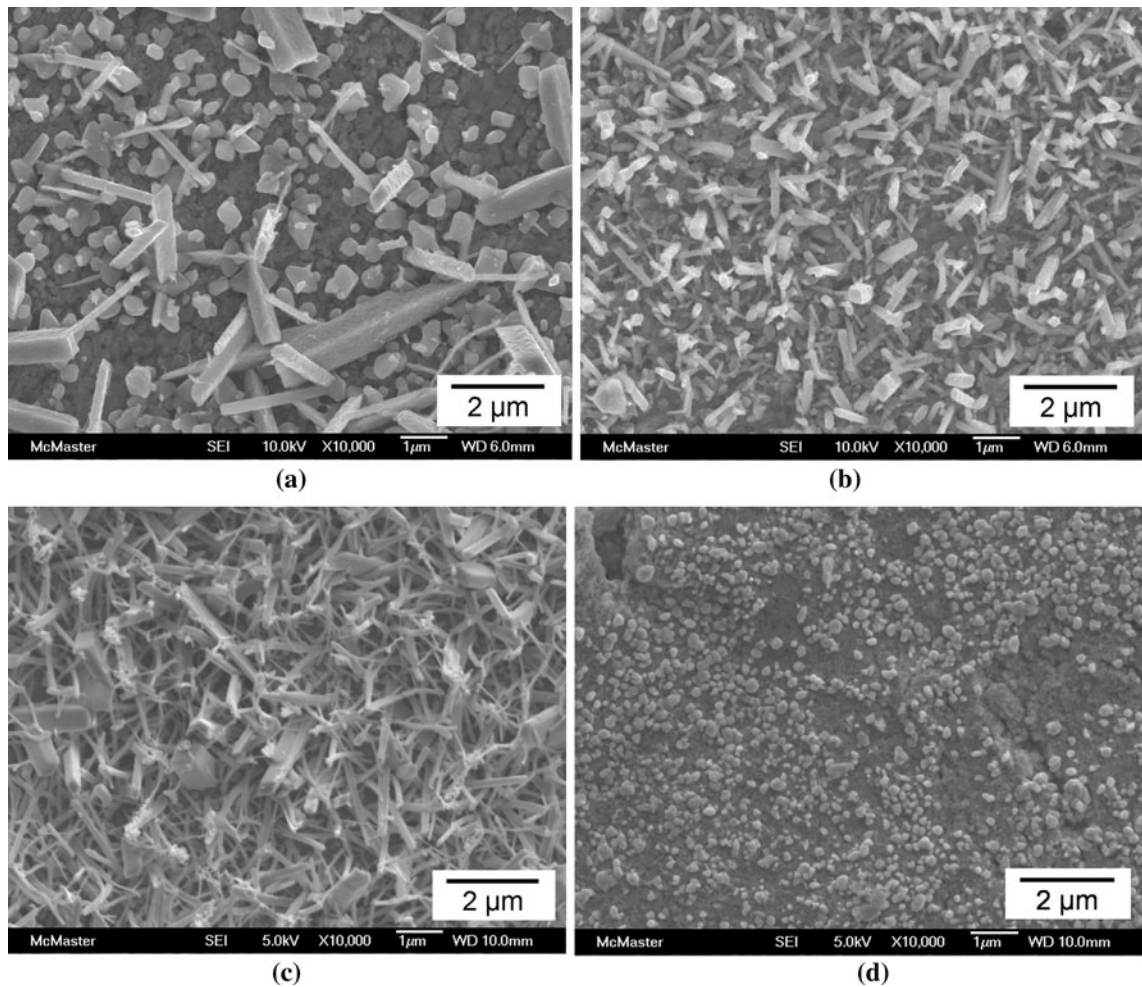


Fig. 10—SEM analysis of the steel/coating interface for the 1.5 pct Si steel (a) $-53\text{ }^{\circ}\text{C}$ dp, (b) $-30\text{ }^{\circ}\text{C}$ dp, (c) and (d) $+5\text{ }^{\circ}\text{C}$ dp, (a) through (c) were stripped with 10 pct H_2SO_4 and (d) was stripped with HNO_3 .

to the relatively low stirring in the galvanizing simulator bath, resulting in localized Al depletion. The larger amount of FeZn_{13} at the 278 K ($+5\text{ }^{\circ}\text{C}$) dp could be a result of reduction of iron oxides by Al that may have formed during the IBT and, therefore, present at the steel surface prior to galvanizing. The oxygen partial pressure of the 278 K ($+5\text{ }^{\circ}\text{C}$) dp atmosphere at 738 K ($465\text{ }^{\circ}\text{C}$) was close to the oxygen partial pressure which would result in iron oxidation.^[29]

The reactive wetting mechanism was explored by TEM EDX analysis of the steel coating interface. Two samples with good reactive wetting were analyzed: the 1.0 pct Si $-30\text{ }^{\circ}\text{C}$ dp and 1.5 pct Si $-30\text{ }^{\circ}\text{C}$ dp steels (Figures 11 and 14, respectively). Analysis of these samples gave insight into how good reactive wetting was obtained despite the selective oxidation of the steel surface. The 1.0 pct Si $+5\text{ }^{\circ}\text{C}$ dp steel was also analyzed with TEM on an area that included Zn coverage and a bare spot to investigate the mechanism by which reactive wetting was prevented in the bare area (Figures 12 and 13).

The TEM analysis of the 1.0 pct Si $-30\text{ }^{\circ}\text{C}$ dp steel revealed that Mn and Si rich oxide particles remain at and below the steel surface after galvanizing

(Figure 11(c) through (e) and point a in Table V). These oxide nodules did not form a continuous layer and the Fe_2Al_5 interfacial layer was able to form between the oxide nodules. Fe-Zn intermetallics precipitated on top of the oxides and Fe_2Al_5 (point b in Table V); the Fe-Zn intermetallics were likely FeZn_{13} , as shown by their morphology (Figure 9(b)). Comparison of Figure 3(a) and Figure 11 shows that the morphology of the oxides at the steel surface changed significantly during galvanizing. Before galvanizing (Figure 3(a)), the oxide particles had a spherical cap morphology and after galvanizing the oxides were flattened (Figure 11). The change in oxide morphology suggests dissolution of the oxide in the Zn bath, possibly *via* aluminothermic reduction.

Similar results were observed for the 1.5 pct Si $-30\text{ }^{\circ}\text{C}$ dp steel with Mn and Si rich oxides at and below the steel surface and Fe_2Al_5 forming between surface oxide nodules (Figure 14). Point analyses of the oxides below the steel surface (e and f in Table V) and the Mn map in Figure 14(d) indicate that these subsurface oxides were SiO_2 with a Mn rich shell. This type of core-shell oxide structure has been observed previously in Mn-Si TRIP steels of similar composition.^[47,50]

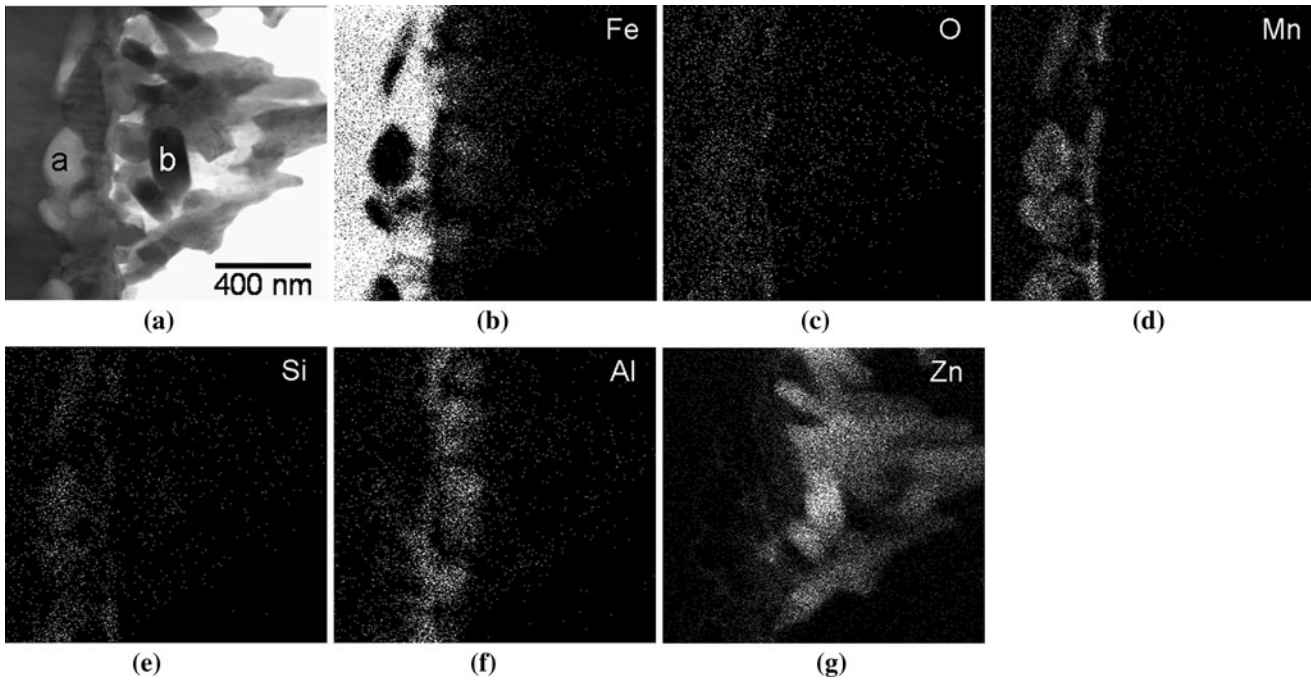


Fig. 11—TEM EDX mapping of the steel/coating interface of the 1.0 pct Si $-30\text{ }^{\circ}\text{C}$ dp steel (a) bright field image, (b) Fe, (c) O, (d) Mn, (e) Si, (f) Al, and (g) Zn maps, quantitative EDX analysis of points a and b in the bright field image is provided in Table V.

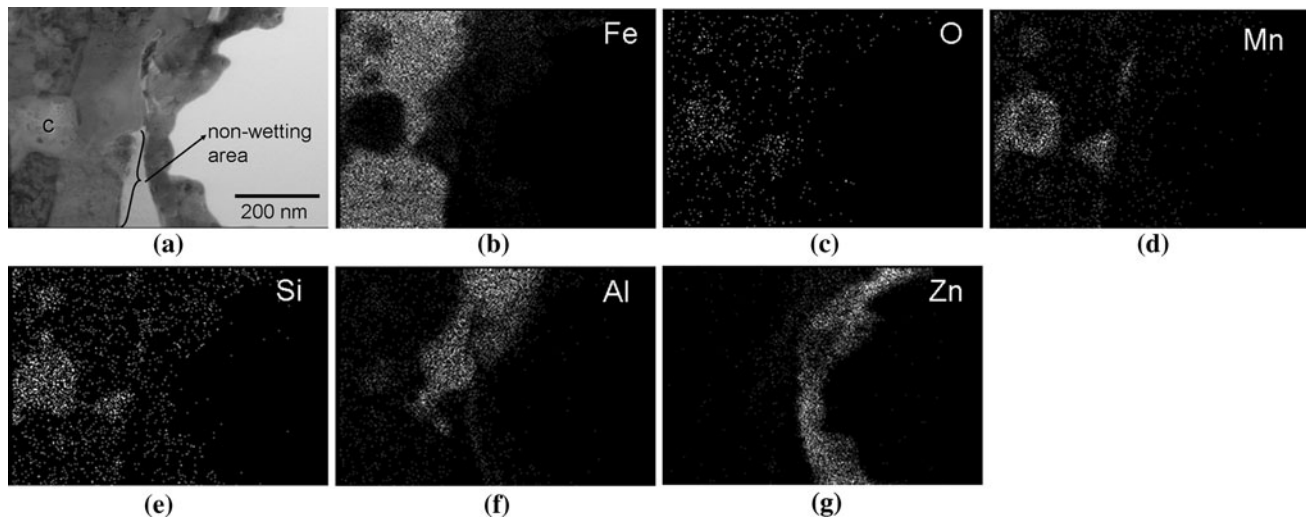


Fig. 12—TEM EDX mapping of the steel/coating interface of the 1.0 pct Si $+5\text{ }^{\circ}\text{C}$ dp steel (a) bright field image, (b) Fe, (c) O, (d) Mn, (e) Si, (f) Al, and (g) Zn maps, quantitative EDX analysis of point c in the bright field image is shown in Table V.

Figure 12 shows a transition area between good and poor reactive wetting for the 1.0 pct Si $+5\text{ }^{\circ}\text{C}$ dp steel. An Al rich interfacial layer was present in the good wetting region in the upper portion of the area analyzed. The Al rich layer did not extend into the bare spot, nor did any Fe-Zn intermetallics. At the start of the bare spot, there were Si and Mn rich oxides at and below the steel surface; oxides such as these were likely the cause of poor wetting. EDX analysis of the middle of the subsurface oxide (point c in Table V) shows that this

oxide is SiO_2 with a Mn rich shell, as shown by the Mn map (Figure 12(d)), similar to the oxides observed below the surface of the 1.5 pct Si $-30\text{ }^{\circ}\text{C}$ dp sample. An area within the bare spot is also shown in Figure 13, where it can be seen that a Mn rich shell (Figure 13(d)) is present around an oxide identified as SiO_2 (point d in Table V). There was also a Mn, Si, and O rich region at the surface, which is likely a thin film of Mn_2SiO_4 , in agreement with the XPS results. This oxide was likely what prevented reactive wetting in this area.

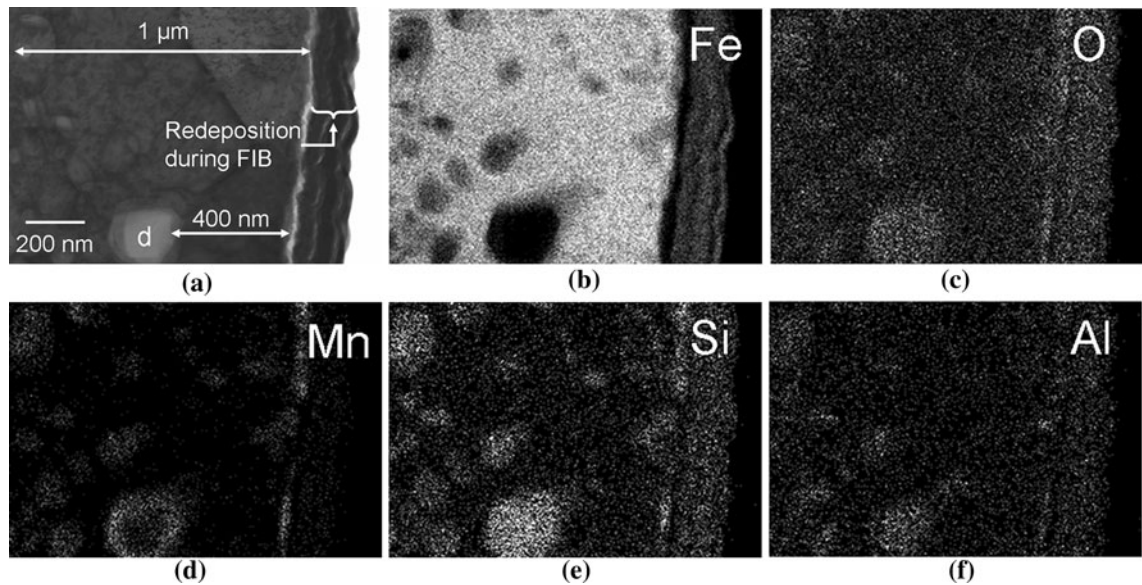


Fig. 13—TEM EDX mapping of the steel surface within a bare spot on the 1.0 pct Si +5 °C dp galvanized steel (a) bright field image, (b) Fe, (c) O, (d) Mn, (e) Si, and (f) Al maps, quantitative EDX analysis of point d in the bright field image is shown in Table V.

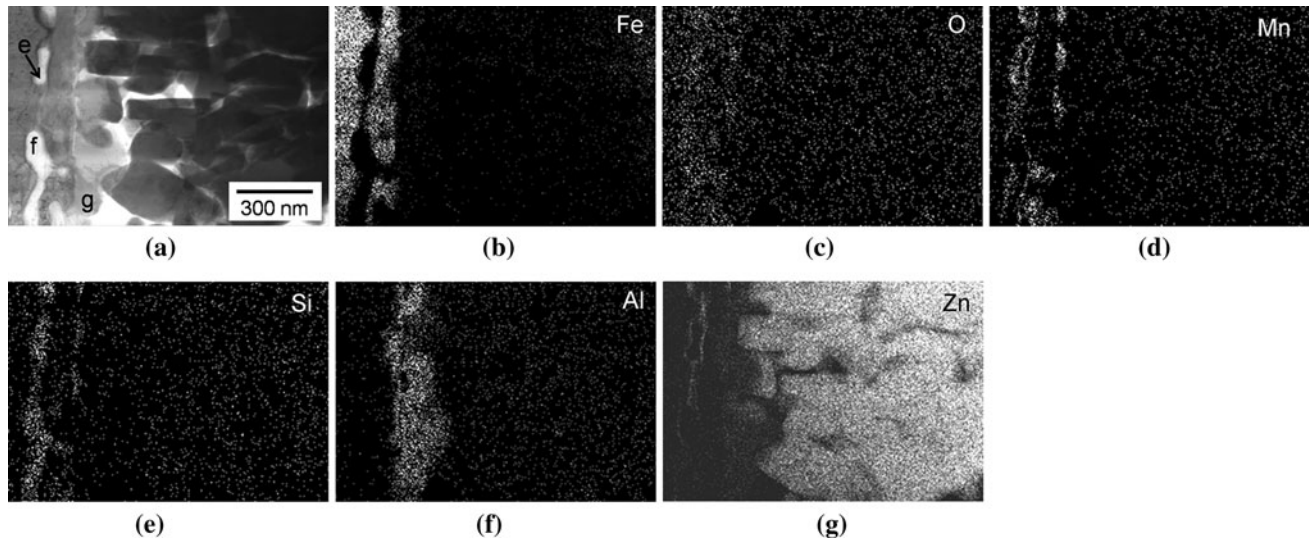


Fig. 14—TEM EDX mapping of the steel/coating interface of the 1.5 pct Si -30 °C dp steel (a) bright field image, (b) Fe, (c) O, (d) Mn, (e) Si, (f) Al, and (g) Zn maps, quantitative EDX analysis of points e, f, and g in the bright field image is provided in Table V.

Table V. Quantitative EDX Analysis of Points a through g Indicated in STEM Bright Field Images (Figures 11 through 14(a)) (Atomic Percent)

Point	Fe	Zn	Al	Mn	O	Si	Phase Present
a	4.11	1.46	4.37	21.51	22.41	42.41	mixed Mn-Si oxide
b	8.67	86.06	0.74	0.07	0.14	0.80	FeZn ₁₃
c	18.35	0.99	9.25	5.47	44.03	21.55	SiO ₂
d	5.67	0.39	2.14	1.85	55.44	35.14	SiO ₂
e	5.98	1.40	0.21	0.86	58.40	33.15	SiO ₂
f	5.83	1.07	0.17	0.02	60.01	32.89	SiO ₂
g	36.97	9.99	46.71	0.02	5.95	0.37	Fe ₂ Al ₅ Zn _x

V. CONCLUSIONS

The objectives of the present research were to study the effect of oxygen partial pressure on surface chemistry, oxide morphology, and reactive wetting for a 1.5 pct Si and a 1.0 pct Si-0.5 pct Al TRIP steel. For both steels and all three annealing atmospheres, considerable enrichment of Mn and Si in the form of oxides was observed at the steel surface after annealing prior to galvanizing. Similar trends were observed when comparing the 1.0 pct Si steel and 1.5 pct Si steel with respect to oxygen partial pressure of the annealing atmosphere. Si enrichment at the steel surface was highest at the lowest oxygen partial pressure, and Si enrichment of the steel surface decreased with increasing oxygen partial pressure. Mn enrichment was the highest at the 243 K (−30 °C) dp for both TRIP steel compositions. The oxygen partial pressure of the annealing atmosphere also affected the oxide species present on the steel surface and the oxide morphology. In terms of the predominant Si containing oxide species, SiO₂ was favored at the lowest oxygen partial pressure annealing atmosphere (220 K (−53 °C) dp or 223 K (−50 °C) dp) and Mn₂SiO₄ was favored at the highest (278 K (+5 °C) dp). For the 1.0 pct Si steel using the 223 K (−50 °C) dp and 243 K (−30 °C) dp annealing atmospheres, the predominant oxide morphology comprised larger nodules at the steel surface and between these nodules were regions of metallic Fe. For the 1.0 pct Si +5 °C dp steel, the nodules were smaller and more closely spaced. For the 1.5 pct Si −53 °C dp steel, there were nodules, some large and some very small that appear as a film at lower magnifications. For the 1.5 pct Si −30 °C dp steel, a mixture of oxide morphologies was observed. Some grains had large oxide nodules with a Si rich film between the nodules and other grains had small nodules that formed a film type oxide. For the 1.5 pct Si +5 °C dp steel, the oxide nodules were small and closely spaced, similar to the morphology obtained for the 1.0 pct Si +5 °C dp steel.

Good reactive wetting was observed for both steel chemistries at the 220 K (−53 °C) dp or 223 K (−50 °C) dp and the 243 K (−30 °C) dp. Good reactive wetting was attributed to the oxide morphology as Fe₂Al₅ could form between the more widely spaced, larger oxide nodules. For the 1.5 pct Si −53 °C dp and −30 °C dp steels, where very small oxide nodules or film type oxides were observed, good wetting was attributed to the thin nature of these oxides. At the 278 K (+5 °C) dp, poor wetting was observed for both steel chemistries with a large number of bare spots present in the Zn overlay. Poor wetting at the 278 K (+5 °C) dp was attributed to the more closely spaced oxide nodules impeding the formation of Fe₂Al₅.

ACKNOWLEDGMENTS

The authors thank U.S. Steel Canada, Xstrata Zinc Canada, the Natural Sciences and Engineering Research Council of Canada (NSERC), and the members of the McMaster Steel Research Centre for their

financial support. We also thank the following people from McMaster: Jason Lavallée, John Thomson, Fred Pearson, Carmen Andrei, and Julia Huang. We also thank Li Sun (ArcelorMittal Dofasco) for XPS analysis, Shihong Xu (ACSES, the Alberta Centre for Surface Engineering and Science) for the Auger analysis, and the Academic User Access Facility (AUA) program of the CANMET Materials Technology Laboratory for the fabrication of the TRIP steels.

REFERENCES

1. M. Takahashi, H. Yoshida, and S. Hiwatahi: *Int. Conf. on TRIP-Aided High Strength Ferrous Alloys*, Ghent, Belgium, June 19–21, 2002, pp. 103–11.
2. B. Mintz: *Int. Mater. Rev.*, 2001, vol. 46, pp. 169–97.
3. J. Van Slycken, P. Verleysen, J. Degrieckm, J. Bouquerel, and B.C. De Cooman: *Mater. Sci. Eng. A*, 2007, vols. 460–461, pp. 516–24.
4. B.C. De Cooman: *Curr. Opin. Solid State Mater. Sci.*, 2004, vol. 8, pp. 285–303.
5. V.F. Zackay, E.A. Parler, D. Fahr, and R. Busch: *Trans. ASM*, 1967, vol. 60, pp. 252–59.
6. P. Jacques, X. Cornet, P. Harlet, J. Ladrière, and F. Delannay: *Metall. Mater. Trans. A*, 1998, vol. 29A, pp. 2383–93.
7. O. Matsumura, Y. Sakuma, and H. Takechi: *Trans. ISIJ*, 1987, vol. 27, pp. 570–79.
8. P. Jacques, Q. Furnémont, S. Godet, T. Pardoën, K. Conlon, and F. Delannay: *Philos. Mag.*, 2006, vol. 86, pp. 2371–92.
9. P.J. Jacques, E. Girault, P. Harlet, and F. Delannay: *ISIJ Int.*, 2001, vol. 41, pp. 1061–67.
10. Y. Tomota, H. Tokuda, Y. Adachi, M. Wakita, A. Moriai, and Y. Morii: *Acta Mater.*, 2004, vol. 52, pp. 5737–45.
11. P. Jacques, Q. Furnémont, A. Mertens, and F. Delannay: *Phil. Mag. A*, 2001, vol. 81, pp. 1789–1812.
12. P.J. Jacques, E. Girault, A. Mertens, B. Verlinden, J. Van Humbeeck, and F. Delannay: *ISIJ Int.*, 2001, vol. 41, pp. 1068–74.
13. S. Takeuchi: *J. Phys. Soc. Jpn.*, 1969, vol. 27, pp. 929–40.
14. F.B. Pickering: *Physical Metallurgy and the Design of Steels*, Applied Science Publishers Ltd., London, 1978, p. 11.
15. E. Girault, P. Jacques, P. Ratchev, J. Van Humbeeck, B. Verlinden, and E. Aernoud: *Mater. Sci. Eng. A*, 1999, vols. 273–275, pp. 471–74.
16. A. Pichler, S. Traint, G. Arnolder, P. Stiaszny, M. Blaimschein, and E.A. Werner: *Iron Steelmaker*, 2003, vol. 30, pp. 21–31.
17. A. Mertens and J. McDermid: *Materials Science & Technology 2005—Developments in Sheet Products for Automotive Applications*, Pittsburgh, PA, Sept. 25–28, 2005, The Minerals, Metals and Materials Society (TMS), Warrendale, PA, 2005, pp. 199–210.
18. D. Krizan, B.C. De Cooman, and J. Antonissen: *International Conference on Advanced High Strength Sheet Steels for Automotive Applications Proceedings*, Winter Park, CO, June 6–9, 2004, Association for Iron and Steel Technology, Warrendale, PA, 2004, pp. 205–16.
19. E.M. Bellhouse and J.R. McDermid: *Metall. Mater. Trans. A*, 2010, DOI: 10.1007/s11661-010-0185-7.
20. P. Drillet, Z. Zermout, D. Bouleau, J. Maigne, and S. Claessens: *Proc. 6th Int. Conf. on Zinc Alloy Coated Steel Sheet*, Chicago, IL, Apr. 4–7, 2004, Association for Iron and Steel Technology, Warrendale, PA, pp. 1123–34.
21. J. Mahieu, S. Claessens, and B.C. De Cooman: *Metall. Mater. Trans. A*, 2001, vol. 32A, pp. 2905–08.
22. J. Maki, J. Mahieu, B.C. De Cooman, and S. Claessens: *Mater. Sci. Technol.*, 2003, vol. 19, pp. 125–31.
23. J. Mahieu, S. Claessens, B.C. De Cooman, and F. Goodwin: *Proc. 6th Int. Conf. on Zinc Alloy Coated Steel Sheet*, Chicago, IL, Apr. 4–7, 2004, Association for Iron and Steel Technology, Warrendale, PA, 2004, pp. 529–38.
24. J. Mahieu, B.C. De Cooman, J. Maki, and S. Claessens: *Iron Steelmaker*, 2002, vol. 29, pp. 29–34.
25. J. Mahieu, S. Claessens, B.C. De Cooman, and F. Goodwin: *MS&T 2004 Conf. Proc.*, New Orleans, LA, Sept. 26–29, 2004,

- The Minerals, Metals and Materials Society (TMS), Warrendale, PA, 2004, pp. 847–57.
26. E.M. Bellhouse, A.I.M. Mertens, and J.R. McDermid: *Mater. Sci. Eng. A*, 2007, vol. 463, pp. 147–56.
 27. E.M. Bellhouse and J.R. McDermid: *MS&T 2007 Conf. Proc. - Automotive Zinc Coated Steel Sheets*, Detroit, MI, Sept. 16–20, 2007, The Minerals, Metals and Materials Society (TMS), Warrendale, PA, 2007, pp. 547–56.
 28. J.R. McDermid, M.H. Kaye, and W.T. Thompson: *Metall. Mater. Trans. B*, 2007, vol. 38B, pp. 215–30.
 29. H.A. Fine and G.H. Geiger: *Handbook on Material and Energy Balance Calculations in Metallurgical Processes*, TMS-AIME, Warrendale, PA, 1979, pp. 428–431.
 30. J. Finster: *Surf. Interface Anal.*, 1988, vol. 12, pp. 309–14.
 31. I. Parezanović and M. Spiegel: *Steel Res. Int.*, 2005, vol. 76, pp. 832–39.
 32. X. Vanden Eynde, J.P. Servais, and M. Lamberigts: *Proc. 6th Int. Conf. on Zinc Alloy Coated Steel Sheet*, Chicago, IL, Apr. 4–7, 2004, Association for Iron and Steel Technology, Warrendale, PA, 2004, pp. 361–72.
 33. T. Van De Putte, D. Loison, J. Penning, and S. Claessens: *Metall. Mater. Trans. A*, 2008, vol. 39A, pp. 2875–84.
 34. W.H. Casey, M.F. Hochella, Jr., and H.R. Westrich: *Geochim. Cosmochim. Acta*, 1993, vol. 57, pp. 785–93.
 35. B.R. Strohmeier and D.M. Hercules: *J. Phys. Chem.*, 1984, vol. 88, pp. 4922–29.
 36. C. Wagner: *Z. Elektrochem.*, 1959, vol. 63, pp. 772–82.
 37. J.M. Maigne, M. Lamberigts, and V. Leroy: in *Developments in the Annealing of Sheet Steels*, R. Pradhan and I. Gupta, eds., TMS, Warrendale, PA, 1992, pp. 512–28.
 38. C.R. Shastri, J.A. Rotole, and T.W. Kaiser: *Proc. 7th Int. Conf. on Zinc and Zinc Alloy Coated Steel Sheet*, Osaka, Japan, Nov. 18–22, 2007, Iron and Steel Institute of Japan, Tokyo, Japan, 2007, pp. 403–08.
 39. D. Huin, V. Lanteri, D. Loison, P. Autesserre, and H. Gaye: *Microscopy of Oxidation 3, Proc. 3rd Int. Conf. on the Microscopy of Oxidation*, S.B. Newcomb and J.A. Little, eds., University of Cambridge, Cambridge, United Kingdom, 1996, pp. 573–86.
 40. D. Huin, P. Flauder, and J.-B. Leblond: *Oxid. Met.*, 2005, vol. 64, pp. 131–67.
 41. *Diffusion Data*, 1969, vol. 3, p. 270.
 42. J. Takada, S. Yamamoto, S. Kikuchi, and M. Adachi: *Oxid. Met.*, 1986, vol. 25, pp. 93–105.
 43. J. Takada and M. Adachi: *J. Mater. Sci.*, 1986, vol. 21, pp. 2133–37.
 44. H. Oikawa: *Technol. Rep. Tohoku Univ.*, 1983, vol. 48, pp. 7–77.
 45. R.J. Borg and D.Y.F. Lai: *J. Appl. Phys.*, 1970, vol. 41, pp. 5193–5200.
 46. J. Takada, K. Kashiwagi, and M. Adachi: *J. Mater. Sci.*, 1984, vol. 19, pp. 3451–58.
 47. Y.F. Gong, H.S. Kim, and B.C. De Cooman: *ISIJ Int.*, 2008, vol. 48, pp. 1745–51.
 48. R. Khondker, A. Mertens, and J.R. McDermid: *Mater. Sci. Eng. A*, 2007, vol. 463, pp. 157–65.
 49. Y.F. Gong, T.J. Song, H.S. Kim, J.H. Kwak, and B.C. De Cooman: *Proc. Asia-Pacific Galvanizing Conf. 2009*, Jeju, Korea, Nov. 8–12, 2009, The Corrosion Science Society of Korea, Seoul, Korea, 2009, paper no. B-15.
 50. X.S. Li, S.-I. Baek, C.-S. Oh, S.-J. Kim, and Y.-W. Kim: *Scripta Mater.*, 2007, vol. 57, pp. 113–16.